Assessing Seaglider Model-Based Position Accuracy on an Acoustic Tracking Range

JAMES S. BENNETT,[a] FREDERICK R. STAHR,[a] CHARLES C. ERIKSEN,[a] MARTIN C. RENKEN,[b] WENDY E. SNYDER,[b] AND LORA J. VAN UFFELEN[c]

[a] *School of Oceanography, University of Washington, Seattle, Washington*
[b] *Naval Undersea Warfare Center Keyport Division, Keyport, Washington*
[c] *Department of Ocean Engineering, University of Rhode Island, Narragansett, Rhode Island*

(Manuscript received 18 June 2020, in final form 31 March 2021)

ABSTRACT: Seagliders are buoyancy-driven autonomous underwater vehicles whose subsurface position estimates are typically derived from velocities inferred using a flight model. We present a method for computing velocities and positions during the different phases typically encountered during a dive–climb profile based on a buoyancy-driven flight model. We compare these predictions to observations gathered from a Seaglider deployment on the acoustic tracking range in Dabob Bay (200 m depth, mean vehicle speeds $\sim$30 cm s^{-1}), permitting us to bound the position accuracy estimates and understand sources of various errors. We improve position accuracy estimates during long vehicle accelerations by numerically integrating the flight model's fundamental momentum-balance equations. Overall, based on an automated estimation of flight-model parameters, we confirm previous work that predicted vehicle velocities in the dominant dive and climb phases are accurate to $<$1 cm s^{-1}, which bounds the accumulated position error in time. However, in this energetic tidal basin, position error also accumulates due to unresolved depth-dependent flow superimposed upon an inferred depth-averaged current.

KEYWORDS: Profilers, oceanic; Laboratory/physical models; Model evaluation/performance

1. Introduction

Autonomous underwater gliders, such as the University of Washington Seaglider, have been routinely used for decades to collect physical, chemical, and biological oceanographic data during deployments to various ocean basins lasting days to over a year. Recently, there has been interest in using gliders as a platform for acoustic receiving (Van Uffelen et al. 2013, 2016). Gliders equipped with acoustic receiving devices can complement or be used in place of more traditional, and more expensive, moored systems or ship-based receivers. However, particularly for measurements of active acoustic transmissions, it is important to have precise positioning of the receiver, as position affects source–receiver range, which in turn affects the interpretation of measured acoustic arrival times. Further, proper analysis of mesoscale oceanographic features, such as fronts and eddies, from glider data collected in GPS-denied environments, such as under ice (Webster et al. 2014) or during repetitive subsurface profiles (dive–climb cycles) often requires accurate knowledge of vehicle position.

Glider positions are estimated from vehicle velocities. Recent work has investigated the use of velocimeters or onboard ADCPs to measure vehicle speed directly through the water (Todd et al. 2017; Bennett et al. 2019; Merckelbach et al. 2019). However, in addition to the energy expense, proper interpretation of these data requires an accurate understanding of sensor-mounting geometry and vehicle attack angle, either assumed or inferred from a flight model, to estimate speed along the glide slope (see discussion of attack angle under section 2).

In lieu of these instruments, most vehicle velocities are estimated using a flight model (Eriksen et al. 2001). Prior work assessing the overall accuracy of these estimated glider velocities suggests that flight models can estimate velocities through the water to within 1 cm s^{-1} both vertically (Merckelbach et al. 2010; Frajka-Williams et al. 2011; Rudnick et al. 2013) and horizontally (Todd et al. 2017; Rudnick et al. 2018) in the open ocean. The final estimation of glider position also requires a model or direct measurement of depth-dependent currents acting upon the glider, especially in parts of the ocean with strong current structure. Further, different variants of a flight model (discussed below) may yield different position estimates. For example, a previous study estimated position uncertainties of Seagliders deployed in the Philippine Sea using long-range broadband acoustic signals. The acoustically derived position estimates differed from positions based on flight models by on the order of 650–750 m RMS with a difference of $\sim$100 m RMS between two flight models for 1000-m-deep profiles (Van Uffelen et al. 2016, their Table 1).

To identify and potentially reduce the sources of these positional uncertainties when using a flight model, we deployed a Seaglider on a high-resolution acoustic tracking range, permitting us to bound the positional accuracy of the flight-model approach. Here we describe the method traditionally used to estimate subsurface positions, improve its estimation of velocities and positions, and characterize the magnitude of uncertainty of each component of the method against the ground truth of locations provided by the tracking array. Key to the approach is attention to how vehicle motion is estimated

Supplemental information related to this paper is available at the Journals Online website: https://doi.org/10.1175/JTECH-D-20-0091.s1.

Corresponding author: James S. Bennett, jsb11@uw.edu

DOI: 10.1175/JTECH-D-20-0091.1

© 2021 American Meteorological Society. For information regarding reuse of this content and general copyright information, consult the AMS Copyright Policy (www.ametsoc.org/PUBSReuseLicenses).

Brought to you by University of Washington Libraries | Unauthenticated | Downloaded 06/08/21 05:35 PM UTC

during the distinct phases of glider flight during the profile. In particular, we improve the estimation of velocities and positions during long vehicle accelerations, which historically have been neglected.

2. Data and methods

a. The Dabob Bay deployment

We deployed the University of Rhode Island's Seaglider SG653 in September 2018 on the Dabob Bay acoustic tracking range operated by the Naval Undersea Warfare Center (NUWC) Division Keyport in Washington State (Snyder et al. 2019). The deployment lasted 68 h during which the vehicle completed 86 profiles. Target profile depths varied between 45 and 126 m depending on the water depth and desire to avoid bottom-mounted tracking range gear. Profiles typically lasted ~45 min and covered ~500 m over ground, attaining a mean vehicle speed of ~30 cm s^{-1}. To record flight headings and vehicle pitch, in-water compass calibration profiles were performed to calibrate the onboard Sparton digital compass (model SP3003D). Analysis of heading turn rates indicates the accuracy of reported headings was within 1°. GPS locations were recorded by the vehicle at the beginning and end of each profile. The average position uncertainty reported by the Garmin GPS engine (model 15H-W) was 8.3 m. The vehicle was instrumented with a variety of standard and experimental sensors in addition to the acoustic pinger used by the tracking range.

The Dabob Bay facility (12 km long, 2.5 km wide, 200 m deep) is instrumented with a series of short-baseline acoustic tracking arrays that were used to locate the Seaglider during daytime operations. Due to various tracking-range restrictions only 16 profiles had acoustic tracking through their entirety (the ''tracked profiles''). The range operates by using differences in time of receipt of a synchronized acoustic ping from the vehicle by clusters of hydrophones at known locations to estimate position based on sound velocity through the water. The ping encodes a phase-shift key enabling high temporal resolution and superior rejection of any hull-coupled reemissions of the ping.

The pinger was resynchronized ~45.5 h after the start of the deployment and required a 0.1 s adjustment to the ping time, indicating a small pinger clock drift. Under a constant ping interval assumption (nominally every 4 s), the error in travel time measured by the range tracking system grows linearly with the number of pings from the time of synchronization. The resulting localization error is then related to this travel time error by sound speed. The expected tracking error was corrected based on sound speed estimated from a conductivity–temperature–depth (CTD) cast conducted by the range during the deployment. Ray bending effects in this shallow (~200 m) basin are estimated to be negligible.

Once drift corrections were applied and smoothing of range-acquired positions was performed due to known acoustic issues yielding slight timing mismatches, the horizontal acoustic tracking uncertainty is estimated to be less than 1 m, consistent with the range operator's reports. However, due to the track array geometry, the vertical acoustic tracking uncertainty (>5 m) is larger than the vertical track location uncertainty using depth inferred from the Seaglider's pressure sensor (Kistler model 4260M060, <1 m uncertainty); therefore, the latter was used for all vertical positions.

Dabob Bay, part of Hood Canal and the Salish Sea, experiences substantial tidal exchanges. The tracked profiles appear to cover at least one complete semidiurnal ebb–flood cycle. However, no independent measurements of tidal height or current were obtained on the range during the deployment, which limits our ability to independently model those motions. Tidal models (NOAA 2020) of Dabob Bay suggest a height change of 2 m during the tracked portion of the deployment with estimated tidal currents of 2 cm s^{-1}.

Using three-dimensional positions and time stamps from the aligned track data, vehicle track speed components were computed by taking the center-first difference between successive estimates. Speed magnitude along the vehicle flight track is computed as the square root of the sum of the squared speed components. These speeds were interpolated from the track time grid to the nearest glider time sample, allowing comparison with the speed estimates from the method described below.

b. A method for estimating Seaglider positions by profile phase

Direct measurement of vehicle speed and location along its glide path is typically unavailable. Although measured rate of change of pressure provides an indication of a vehicle's vertical velocity (rise/fall rate), horizontal velocity estimates are flight model based, from which displacements and hence locations are derived relative to a GPS fix at profile start. Further, the vehicle undergoes several substantial periods of drift and acceleration that must be accounted for in addition to the errors in GPS location. We describe the phase-based method that accounts for these different flight regimes for typical Seaglider profiles.

A typical Seaglider profile consists of several distinct *phases* (see Fig. 1, top panel):

- an *initial surface drift* phase during which the vehicle, positively buoyant and pitched steeply downward, acquires a starting GPS fix, optionally loiters to collect surface observations before engaging the variable buoyancy device (VBD) to become negatively buoyant,
- a *flare* phase during which the increasingly negatively buoyant vehicle accelerates steeply downward from the surface rapidly before ''flaring'' to its desired downward glide pitch angle,
- the *dive* phase during which the vehicle flies steadily at a desired vertical speed and glide slope,
- an *apogee* phase, starting when the vehicle reaches a predetermined depth, during which it pitches to a shallower downward angle (typically −5° from horizontal) and pumps the VBD system to become neutrally buoyant, decelerating to zero vertical speed but maintaining some forward speed,
- an optional *loiter* phase during which the vehicle drifts, collecting data at the apogee depth,

Brought to you by University of Washington Libraries | Unauthenticated | Downloaded 06/08/21 05:35 PM UTC

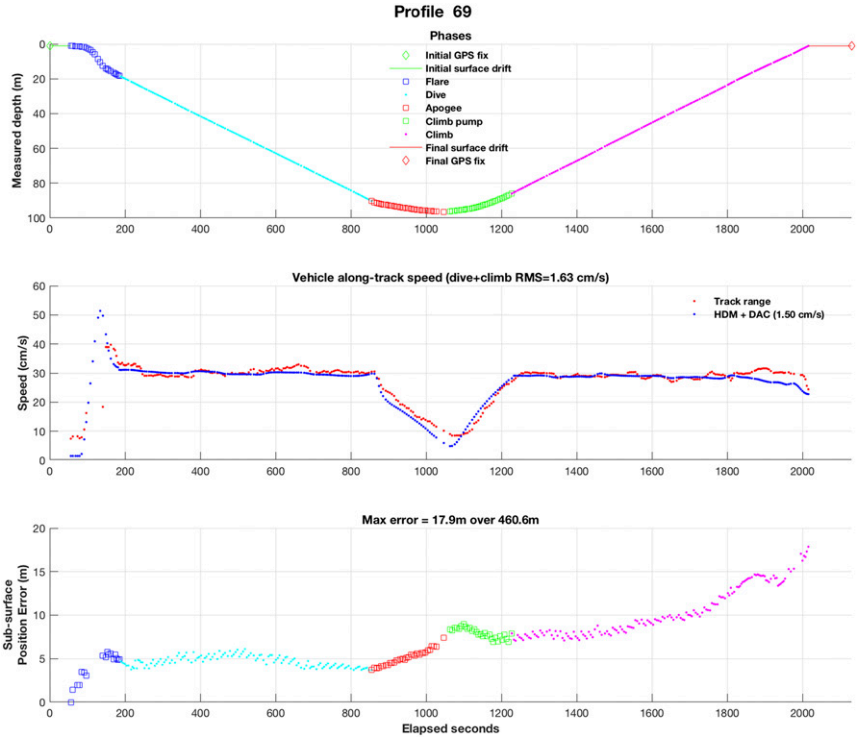

FIG. 1. (top) Depth vs time and phase structure for profile 69. (middle) Along-track speeds from both acoustic tracking-range (red) and method predictions (blue) for same profile. (bottom) Subsurface position error marked by phase. See main text for definitions and discussion.

- a *climb pump* phase during which the vehicle pitches upward to achieve the desired glide slope and pumps to increase buoyancy, accelerating the vehicle,
- the *climb* phase during which the vehicle once again flies steadily at the desired vertical speed and glide slope toward the surface, and
- a *final surface drift* phase that begins when the vehicle achieves a preset shallow depth (typically ~2 m) and during which it pitches fully down, increases buoyancy to expose the antenna, gathers a final GPS fix, and finalizes the data files, marking the end of the profile.

The vehicle speed during each phase is modeled and estimated differently. The velocity of the initial surface drift (and surface loiter) phase is computed from the differences between the GPS fixes of previous surfacing and profile start. The final surface drift phases as well as any apogee loiter phase are assumed to have no speed through the water. A buoyancy-driven "hydrodynamic" flight model (HDM; Eriksen et al. 2001), summarized briefly below, estimates the horizontal and vertical speed during all other phases.

c. *The flight model*

Consider a Seaglider flying at a given glide angle θ measured positive anticlockwise from horizontal as shown in Fig. 2. Given forces (units: N) of lift L normal to the glide slope (of sign opposite to θ), drag D opposing vehicle velocity, and buoyancy B (of the same sign as θ), the following momentum-balance equations describe the change in the horizontal U and upward-positive vertical W vehicle speed components relative to water motion, where $W = U\tan\theta$:

$$M\frac{dU}{dt} = -L\sin\theta - D\cos\theta, \tag{1}$$

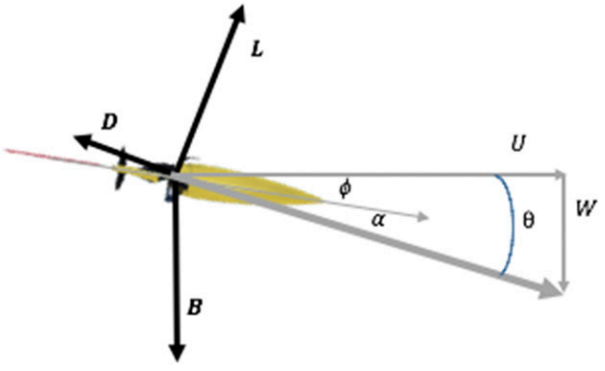

FIG. 2. Diagram of the forces on a Seaglider during the dive phase. Forces are lift (L), drag (D), and buoyancy (B). Glider velocity through the water is U and W in the x and z directions, where θ is the glide angle, ϕ is the measured pitch angle, and α is the attack angle.

Brought to you by University of Washington Libraries | Unauthenticated | Downloaded 06/08/21 05:35 PM UTC

TABLE 1. HDM flight parameters for SG653 in Dabob Bay, September 2018.

Parameter	SG653	Units	Description
a	0.002 238 7	degrees^{-1}	Lift coefficient
b	0.019 109 5	m$^{1/4}$ kg$^{1/4}$ s$^{-1/2}$	Drag coefficient
c	5.7×10^{-6}	degrees^{-2}	Induced drag coefficient
V_0	55 052.1	cm^3	Maximum volume at $T = T_0 = 15$°C, $p = 0$ dbar assuming vehicle mass $M = 55\,783$ g
κ	5.529×10^{-6}	dbar^{-1}	Vehicle compressibility
τ	7.05×10^{-5}	°C^{-1}	Vehicle thermal expansion

$$M\frac{dW}{dt} = B + L\cos\theta - D\sin\theta. \tag{2}$$

Lift and drag forces are assumed to take the bulk formula forms:

$$L = ql^2a\alpha, \tag{3}$$

$$D = ql^2(bq^s + c\alpha^2), \tag{4}$$

where a is the lift coefficient, α the attack angle, b the drag coefficient, c the induced drag coefficient, q the dynamic pressure, and s is a parameter specifying departure of drag from linear dependence on dynamic pressure ($s = 0$ for a conventional constant drag coefficient). The ratio of lift and drag forces to dynamic pressure have the dimension of area, which we parameterize as l^2; the nominal Seaglider hull length $l = 1.8$ m is used. Dynamic pressure $q = \rho_0(U^2 + W^2)/2$ where ρ_0 is a reference density, here fixed at a nominal 1027.5 kg m^{-3}. Wind tunnel studies established that the Seaglider hull shape has a drag coefficient that varies inversely with the square root of speed such that $s = -1/4$ (Hubbard 1980). The angle of attack α is measured positive anticlockwise from the glide slope, hence of the same sign as lift and opposite sign to buoyancy, vertical velocity, and vehicle pitch angle ϕ. In this convention, pitch angle is the sum of the glide slope angle θ and vehicle angle of attack α, that is, $\phi = \alpha + \theta$, so glide slope angle is always steeper than pitch angle, irrespective of sign.

Vehicle buoyancy B is given by

$$B = g[\rho V(t,p,T) - M], \tag{5}$$

where g is the gravitational acceleration, ρ the in situ water density, M the glider mass, and $V(t, p, T)$ the volume of the glider, which depends on time t, pressure p, and water temperature T. The buoyancy force B results from the difference between the mass of the glider M and the seawater displaced by the glider volume V. The total volume V varies over the course of a profile due to the glider's hydraulically pumped VBD, compressibility of the hull and sensors with pressure, and the expansion of the hull and sensors with temperature:

$$V(t,p,T) = V_{\text{hull}}(t)e^{-[\kappa p - \tau(T-T_0)]}, \tag{6}$$

$$V_{\text{hull}}(t) = (V_0 - \delta V_0) + V_{\text{VBD}}(t), \tag{7}$$

where $V_{\text{VBD}}(t)$ is the volume of the VBD system around a nominal reference point, V_0 is a (computed) total reference volume, T_0 is an arbitrary reference temperature, κ is the overall compressibility of the combined hull, any syntactic foam or foam-filled fairing elements, and sensors for the vehicle, and τ is the volumetric thermal expansion. The term δV_0 captures any unmodeled bias in vehicle volume (hence density) due to, for example, oil expansion with temperature, water uptake by the fiberglass fairing elements, biofouling, etc. In general, there are no independent measurements of long-term uncommanded changes in vehicle density. In this model these changes are reflected as volume changes against an assumed constant mass. Alternatively, these changes could be reflected as changes in mass against a constant volume; this is the approach taken by Rudnick et al. (2013). The convention of subtracting δV_0 from V_0 is arbitrary and historical; increasing δV_0 implies a decrease in overall vehicle volume and hence an increase in its density given constant M.

d. Solutions during steady flight

In steady flight during the dive and climb phases the forces are in balance and dU/dt and dW/dt both vanish. Given an accurate set of flight parameters that characterize the particular vehicle and an estimate of buoyancy B, Eqs. (3) and (4) are

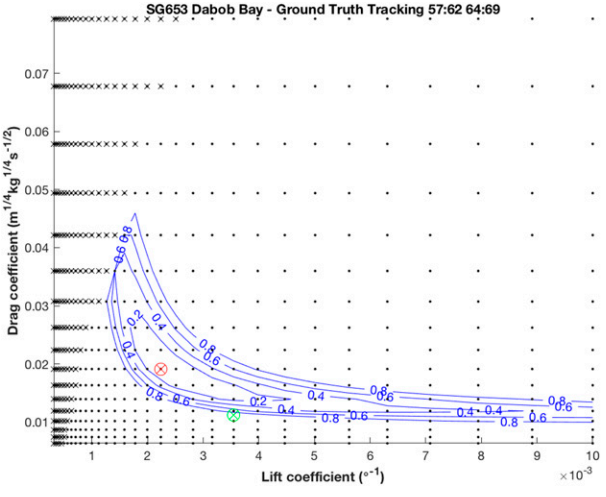

FIG. 3. Lift and drag error estimates for SG653 in Dabob Bay, September 2018. The red circled × indicates the lift–drag pair that minimized the RMS value of the vertical velocities of the combined profiles (0.622 cm s^{-1}). Contours show the difference in expected RMS of measured vs predicted vertical velocity from the minimum value, contoured at an interval of 0.2 up to 0.8 cm s^{-1}. The green circled × indicates the default lift–drag pair for Seagliders carrying a standard instrument package. Black × symbols indicate stalled solutions.

Brought to you by University of Washington Libraries | Unauthenticated | Downloaded 06/08/21 05:35 PM UTC

used to solve iteratively for q and α while satisfying the steady versions of Eqs. (1) and (2). Thus, buoyancy serves to constrain the values of q and α and hence vertical and horizontal speeds. From q and α, the total vehicle speed $\sqrt{U^2 + W^2}$ and glide slope θ are determined.

e. Solutions during accelerated flight

The flare, apogee, and climb pump phases, by contrast, involve lengthy (~2 min) linear VBD-induced accelerations. The steady flight model does not apply during these phases, where buoyancy B and pitch ϕ change rapidly. Historically, motions during these phases have been neglected and velocities were assumed to be zero. Here, however, speed is estimated by solving Eqs. (1) and (2) directly. Substituting Eqs. (3) and (4) yields expressions for the rates of change of U and W over time:

$$\frac{dU}{dt} = \frac{\rho_0 l^2}{2M}[-a\alpha WV - (b + c\alpha^2)UV], \tag{8}$$

$$\frac{dW}{dt} = \frac{B}{M} + \frac{\rho_0 l^2}{2M}[a\alpha UV - (b + c\alpha^2)WV]. \tag{9}$$

Given initial U and W values from rest or the steady flight model and measured ϕ and B, Eqs. (8) and (9) are numerically integrated to find subsequent speed components as well as glide and attack angles.

During the dive and climb phases the vehicle course and speed is controlled through small roll, pitch, and VBD adjustments; the small accelerations induced by them are neglected in estimating vehicle trajectory.

f. Estimating depth-varying currents and final method-predicted speeds

The phase-based method combines the speed estimates for each phase with vehicle heading to estimate horizontal displacement through the water, assuming vehicle velocity direction is that of the compass. These computed displacements provide a prediction of the vehicle's expected surfacing location in still water relative to the starting GPS fix. However, the ocean is rarely still, and the vehicle's surfacing position reflects additional displacements from unmeasured currents that can vary with depth and time over the course of a profile. By default, and in the absence of an alternative model of these currents (or their direct measurement), the difference between the predicted surfacing position and the final GPS position is used to estimate a uniform depth-averaged current (DAC), which is assumed to displace the vehicle horizontally during all phases of the profile, excluding the initial surface drift phase which is directly measured as mentioned previously. Estimates of vehicle horizontal speed over ground and hence location are based on the combination of each phase's relative speed through the water and the DAC estimate. The final estimated along-track speed is based on combined vertical, horizontal, and DAC speeds along the glide path of the vehicle, referred to as the "method-predicted" or "method-estimated" speed below.

g. Estimating flight model parameters

To predict vehicle motion relative to in situ water velocities using the HDM, accurate determination of flight model and buoyancy parameters is required. Using the steady version of (1) with the bulk formula parameterizations (3) and (4) for lift and drag leads to an expression for dynamic pressure:

$$q = \frac{B\sin\theta}{2l^2 bq^s}\left\{1 + \sqrt{1 - \frac{4cbq^s}{a^2\tan^2\theta}}\right\}. \tag{10}$$

Given a set of assumed values of the flight model parameters and measured pitch ϕ and buoyancy B, Eq. (10) can be iteratively solved with ϕ as an initial guess for θ to converge to steady flight model predictions of q, θ, U, and W. Estimation of the flight model parameters is accomplished by a multivariable optimization that minimizes a statistical cost function constructed from multiple realizations of observed values of pitch and buoyancy, typically over multiple profiles (Eriksen et al. 2001). Customarily the cost function has been based on the misfit between observed and predicted vertical velocity W (Frajka-Williams et al. 2011). (The former, of course, neglects water vertical motions such as those due to internal gravity waves, a principal source of the difference.)

Establishing accurate buoyancy parameters, especially the vehicle's maximum volume V_0, is critical to obtaining accurate speed and position estimates based on the hydrodynamic model. If the estimated value of V_0 is, for example, too high, the vehicle will appear less dense and hence more buoyant. Thus, the predicted dive speeds will appear slower and predicted climb speeds will appear faster than actual, leading to rapidly growing position errors during the dive only to improve equally rapidly on the climb.

The appendix describes the automated system used to accurately estimate the flight and buoyancy parameters. Table 1 lists the flight parameters employed to analyze this deployment. The lift and drag parameters were estimated using a subset of the tracked profiles that straddled an ebb–flood cycle to reduce any directional tidal impact on the estimates (Fig. 3). The lift parameter is 63% smaller and the drag parameter is 70% larger than default Seaglider values established by regressions

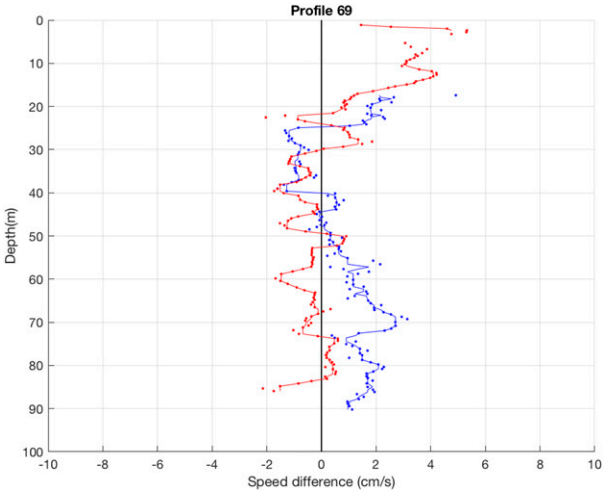

FIG. 4. Difference of acoustically tracked and model-predicted along-track vehicle speeds by depth for dive (blue) and climb (red) phases for profile 69. Solid lines indicate median-filtered differences using 5 samples (25 s). Black line highlights zero speed difference.

Brought to you by University of Washington Libraries | Unauthenticated | Downloaded 06/08/21 05:35 PM UTC

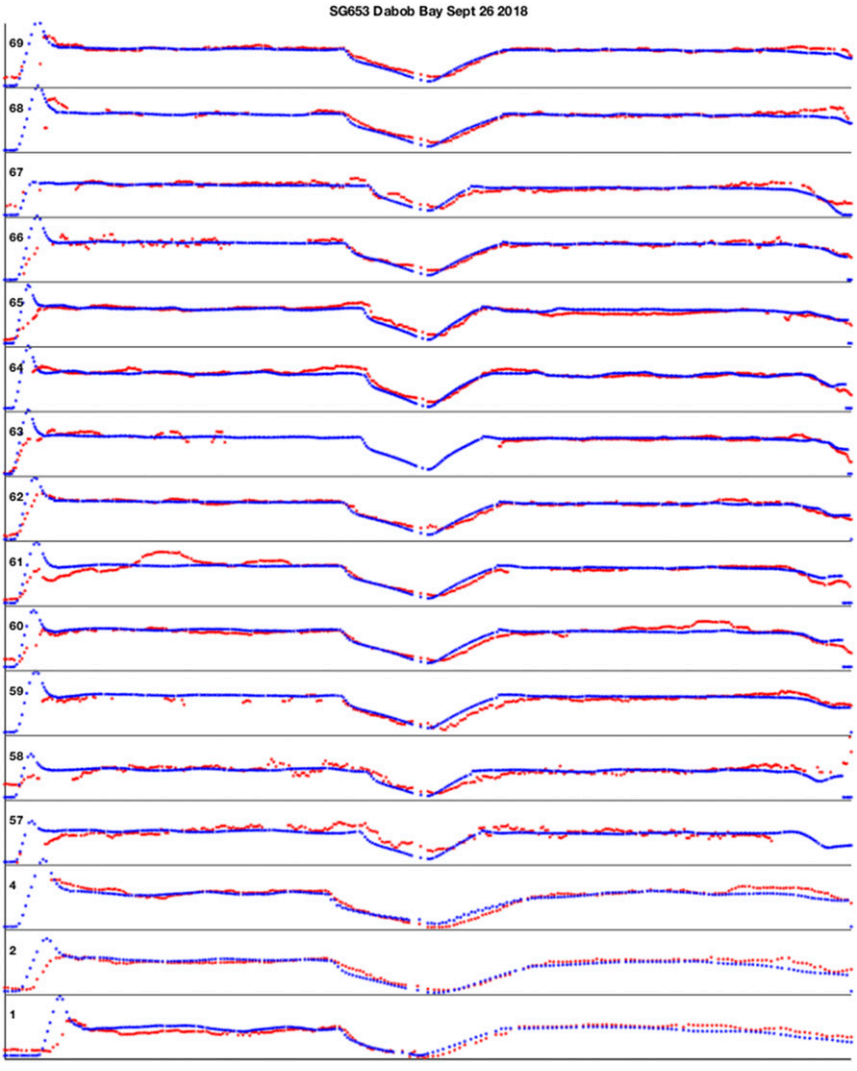

FIG. 5. Speed comparisons for the available acoustically tracked profiles. As in Fig. 1, red points are acoustic-range estimated vehicle speeds; blue points are phase-based method predicted speeds. Each profile's dive and climb phase duration is normalized to 1000 s for ease of comparison. Speeds are not normalized and are offset from the previous profile by 50 cm s^{-1}, indicated by black lines.

over numerous previous deployments. The increased drag parameter for this deployment is consistent with the vehicle carrying several experimental sensors providing significant additional drag elements. Other parameter values are Seaglider defaults, appropriate for this shallow deployment.

h. An alternative model during steady flight

During steady flight, the buoyancy term can be eliminated from the flight model and vehicle speeds can be estimated based solely on measured vehicle vertical velocity and pitch. This variant, called the "glide slope" model (GSM) in Van Uffelen et al. (2016), which also requires an accurate estimate of the lift and drag parameters, is used by Todd et al. (2017) and Rudnick et al. (2018).

Using the steady version of (1) together with (3) and (4) eliminates dependence on buoyancy B, giving

$$c\alpha^2 + a\alpha\tan\theta + bq^s = 0, \tag{11}$$

an equation quadratic in attack angle α. For known values of the flight model parameters a, b, c, and s, glide slope angle θ can be found by iterative solution to the transcendental equation for the root of Eq. (11), given knowledge of pitch angle ϕ, and, in the case $s \neq 0$, vertical speed component W:

$$\phi = \theta - \frac{a\tan\theta}{2c}\left\{1 - \sqrt{1 - \frac{4bc}{a^2\tan^2\theta}\left[\frac{\rho W^2}{2\sin^2\theta}\right]^s}\right\}. \tag{12}$$

Brought to you by University of Washington Libraries | Unauthenticated | Downloaded 06/08/21 05:35 PM UTC

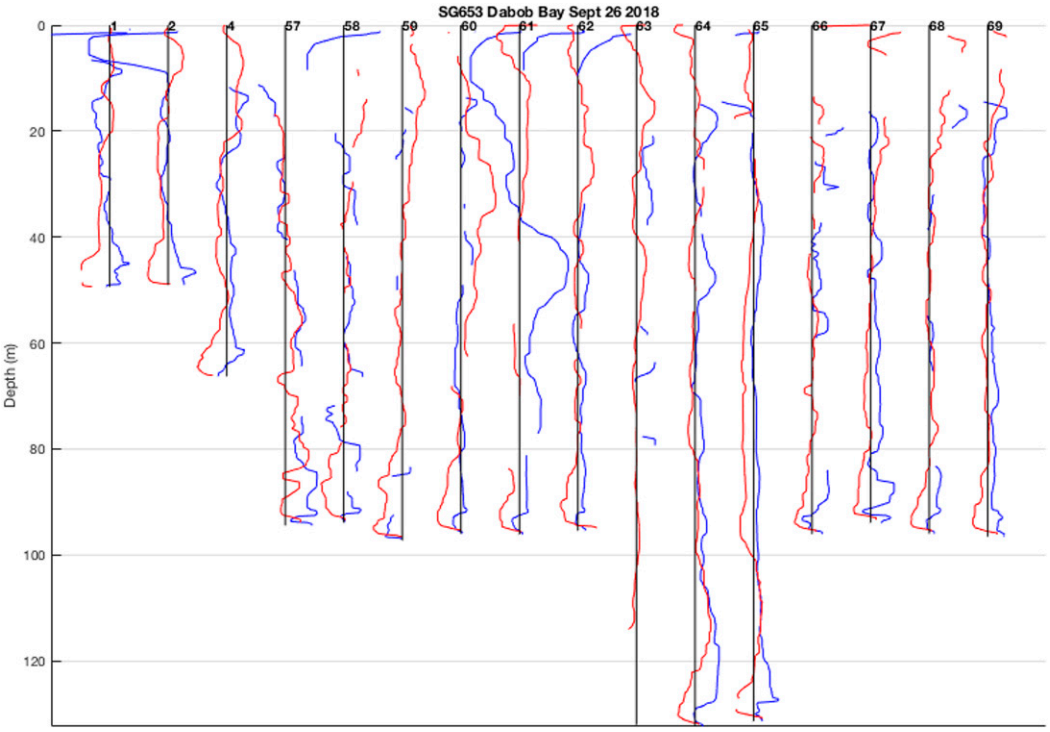

FIG. 6. Median-filtered differences between acoustically tracked and phase-based method predicted vehicle speeds using 5 samples (25 s) for dive (blue) and climb (red) phases by depth for the 16 available acoustically tracked profiles. Black lines indicates zero speed difference for each profile. For the horizontal scale, the distance between vertical black lines represents 15 cm s^{-1}.

Solutions are valid for attack angles such that the discriminant in Eq. (12) is positive. That is, the limiting (stall) attack angle α_s is

$$\alpha_s = -\sqrt{\frac{bq^s}{c}}\frac{\theta}{|\theta|}. \tag{13}$$

This formulation utilizes measured vertical velocity derived from vehicle pressure rate of change, neglecting vertical water velocity. For constant drag coefficient behavior ($s = 0$), the GSM predicts glide slope angle θ without reliance on buoyancy B, while the horizontal speed component U is estimated from glide slope and vertical vehicle speed. The GSM cannot be used, in particular, during the apogee phase because the attack angle becomes large while the pitch approaches the stall angle and the vehicle pressure rate of change becomes small; in this case, the GSM predicts initially accelerating and overall excessive horizontal velocities.

During steady flight, however, the GSM provides nearly identical velocity predictions to the HDM when given the same lift and drag parameters and accurate estimates of buoyancy B. Indeed, significant differences in speeds between the GSM and HDM during the dive and climb phases are diagnostic of misestimation of buoyancy B, typically a poor estimate of V_0 or of incremental changes to δV_0 indicating, for example, biofouling. For example, subsequent reanalysis using the model described here of the Philippine Sea deployment data referenced in the introduction improved the estimates of V_0, bringing the GSM and HDM results into agreement and accounting for the reported ~100 m RMS discrepancy between them. The analysis of the Dabob Bay deployment data here also provided an improved V_0, accounting for the position discrepancies between GSM and HDM reported by Snyder et al. (2019).

Using the GSM to estimate lift and drag parameters requires an alternative constraint to buoyancy utilized by the HDM-based regressions discussed above. Rudnick et al. (2018) observed that the depth-averaged current predicted by adjacent profiles traveling in nearly opposite directions should be the same and used that to compute the implied drag parameter assuming a fixed lift coefficient and angle of attack. This technique, as noted in that work, applies in ocean regimes where the depth-averaged current is expected to be largely constant between the required adjacent profiles, an assumption that may be difficult to achieve in an energetic tidal basin such as Dabob Bay.

Our use of the GSM during Seaglider deployments is expedient. It is employed at the beginning of the deployment to estimate speeds before the vehicle's buoyancy parameters can be determined and it is used by the vehicle for onboard navigation with respect to a depth-averaged current computed from GSM estimates of displacements.

The analysis below makes exclusive use of the HDM.

Brought to you by University of Washington Libraries | Unauthenticated | Downloaded 06/08/21 05:35 PM UTC

3. Results

a. Velocity estimates and position errors in Dabob Bay

The middle panel of Fig. 1 depicts both the along glider-track measured speed (acoustic tracking-range based) and the method-estimated speed, including DAC ($1.50\,\mathrm{cm\,s^{-1}}$), for an example profile. (Similar figures for all tracked profiles are available in the online supplemental data.) The RMS error between the tracking range and method-estimated speeds during the steady dive and climb phases for the profile is $1.63\,\mathrm{cm\,s^{-1}}$. This is largely due to the speed differences seen in Fig. 1 just after flare (200–400 elapsed seconds), just before apogee (600–900 s), and at the end of climb phase (1800–2000 s). These transient velocity differences between the tracking-range and method-based speeds during the dive and climb phases indicate nonconstant currents unaccounted for by the mean DAC assumption. Figure 4 shows the speed discrepancy according to the depth of the profile, indicating a surface-intensified current shallower than 20 m depth.

The changing speed estimates during accelerations are clearly visible in the middle panel of Fig. 1, at the start (flare phase) and in the middle (apogee and climb pump phases) of the profile. Although additional examples in Fig. 5 suggest the flight model captures the speeds during these phases reasonably well, some systematic discrepancies from the tracked speed are apparent that are not easily attributable to unresolved currents, as discussed below.

During the flare phase, the model can misestimate the onset of initial acceleration and tends to overestimate speed before the pitch change just before the dive phase. This is especially obvious in profile 1 and 2 (Fig. 5). The speed overestimation during the flare phase may be due to undetected (unmodeled) trapped air in the aft fairing and antenna stalk causing the (increasingly negative) buoyancy during flare phase to be less negative than is monitored by the vehicle buoyancy engine. Much of this effect is transitory and is less evident in subsequent profiles.

Apogee phase speed is somewhat underestimated and the predicted minimum speed is consistently smaller than observed. It may be that the simple parameterization of form and induced drag fails to describe flight in this regime. As the vehicle moves to its apogee pitch (−5°) and begins decelerating the predicted attack angles become high (approaching 10°), likely slowing it differently than the simple drag parameterization predicts.

Figure 5 shows acoustically tracked versus method-estimated speeds, and Fig. 6 shows the speed differences relative to depth for the 16 tracked profiles of the deployment. Table 2 summarizes the mean differences between acoustically tracked versus method-estimated speeds for the tracked profiles during different phases. As expected, the estimated speeds during the acceleration phases report higher mean differences and standard deviations. The mean method-estimated speeds during dive and climb phases, however, are only slightly underestimated. No consistent velocity discrepancies that might be associated with roll side slip (Todd et al. 2017) were observed.

TABLE 2. Mean differences between acoustically tracked and HDM-estimated speeds for the 16 different tracked profile phases.

Profile phase	Mean speed difference ($\mathrm{cm\,s^{-1}}$)
Flare	−7.0 ± 9.4
Apogee	2.0 ± 2.4
Climb pump	−1.7 ± 2.7
Dive and climb	0.4 ± 2.9

The mean DAC magnitude over the tracked profiles was $2.3 \pm 0.5\,\mathrm{cm\,s^{-1}}$, a nearly 50% reduction compared with a mean DAC magnitude of $4.7 \pm 1.9\,\mathrm{cm\,s^{-1}}$ computed under the historical assumption of zero speed during the acceleration phases. Nonzero speed estimates during the acceleration phases lead to longer predicted distances traveled over ground and hence smaller displacements from predicted surfacing locations to final GPS fixes, reducing DAC magnitudes.

b. Localization estimation and errors in Dabob Bay

Given the method-based speed estimates for the various phases, displacements are computed from the initial GPS position, localizing the vehicle during a profile. We compute the (three-dimensional) distance between the acoustic-range track location and the method-localized solution and observe how the position error changes, reflecting the contributions of velocity discrepancies.

The lower panel of Fig. 1 shows the instantaneous localization error relative to profile start for profile 69. Given the speed differences by depth shown in Fig. 4, the error in position increases near the bottom of the dive phase and then again at the

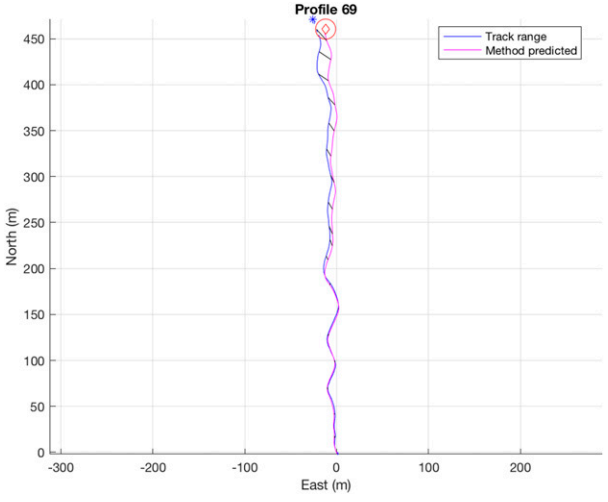

FIG. 7. Position over ground relative to profile 69 start. Acoustic-range surfacing location (blue star) and GPS-determined surfacing location (red diamond) with combined starting and final GPS error shown as red circle. Black lines between tracks indicate corresponding tracking-range positions at same time as phase-based method predicted positions. RMS of position errors is 8.4 m. Maximum position error is 17.9 m (see Fig. 1).

Brought to you by University of Washington Libraries | Unauthenticated | Downloaded 06/08/21 05:35 PM UTC

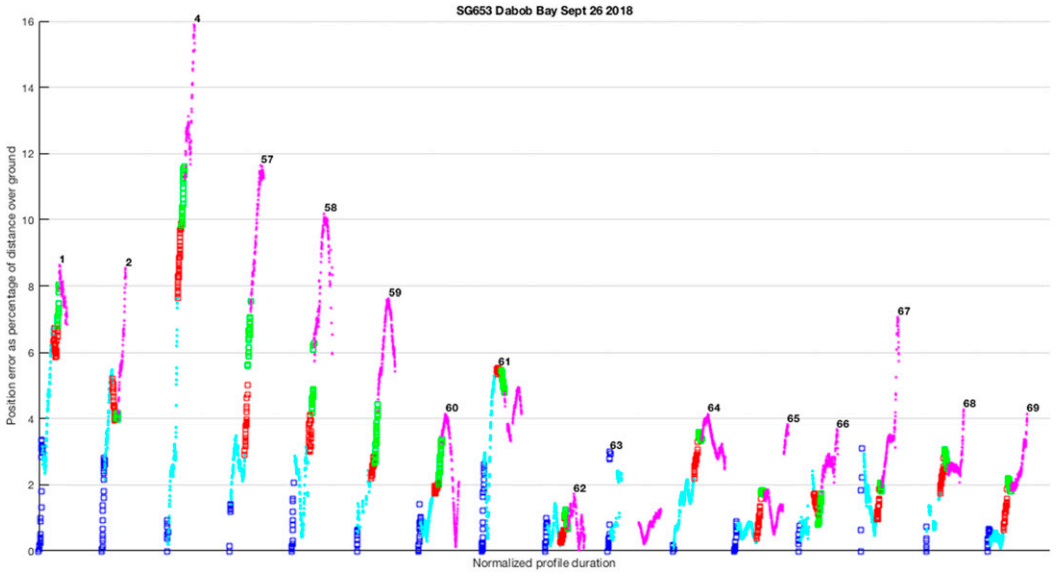

FIG. 8. Relative localization error as a percentage of the tracked distance over ground by profile. Colors and markers are by phase as in Fig. 1. Each profile time is normalized to 3000 s.

top of the climb phase. However, overall the localization error is small (~4% of the 460 m distance covered over ground) as can be seen in the course-over-ground plot for profile 69 in Fig. 7. Relative localization errors expressed as fraction of distance made over ground for all 16 tracked profiles are shown in Fig. 8.

While some of the position errors are due to poor estimates of accelerated flight, most are attributable to transient current

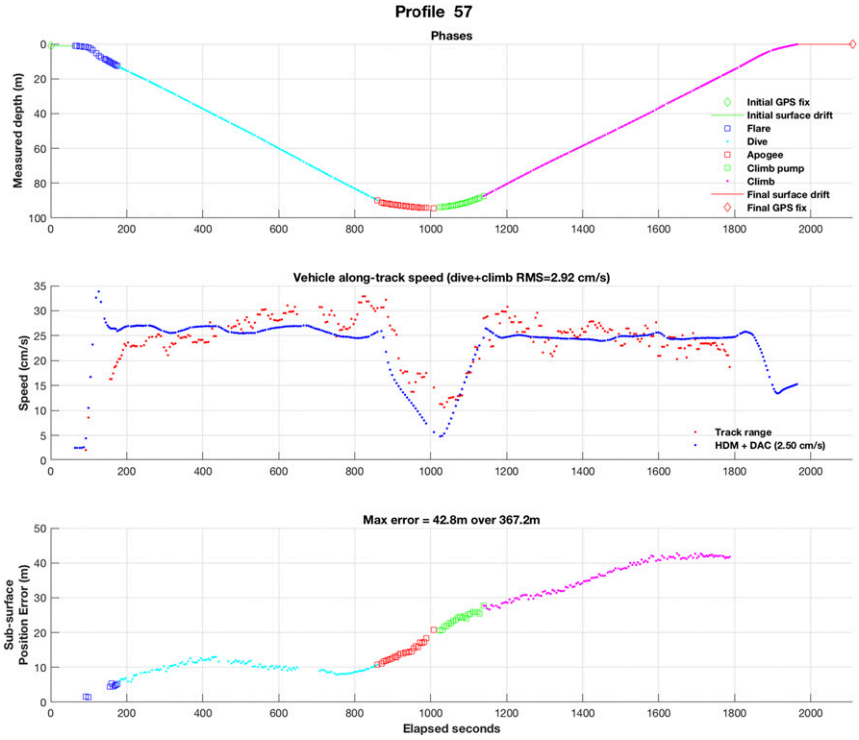

FIG. 9. (top) Depth vs time and phase structure for profile 57. (middle) Measured along-track speeds from both acoustic tracking-range (red) and phase-based method predictions (blue) for same profile. (bottom) Subsurface position error marked by phase.

Brought to you by University of Washington Libraries | Unauthenticated | Downloaded 06/08/21 05:35 PM UTC

variations with depth during dive and climb phases that are on the order of the DAC magnitude. A striking example occurs on profile 57, shown in detail in Fig. 9, with a substantial maximum position error of 13% of the distance over ground. The localization error for this profile is relatively constant until just before apogee when the error abruptly increases, continuing through the apogee and climb pump phases and into the climb phase itself. This is likely due to increased currents deeper than 60 m depth (Fig. 10).

The absolute position estimates (and hence errors) as well as DAC misestimates depend on the accuracy of the GPS fixes at the start and end of the profile. As mentioned, the average GPS fix error for this deployment was on the order of 8.3 m, adding a potential $8.3\sqrt{2} = 11.7$ m overall absolute position error to these estimates based on the two independent measurements.

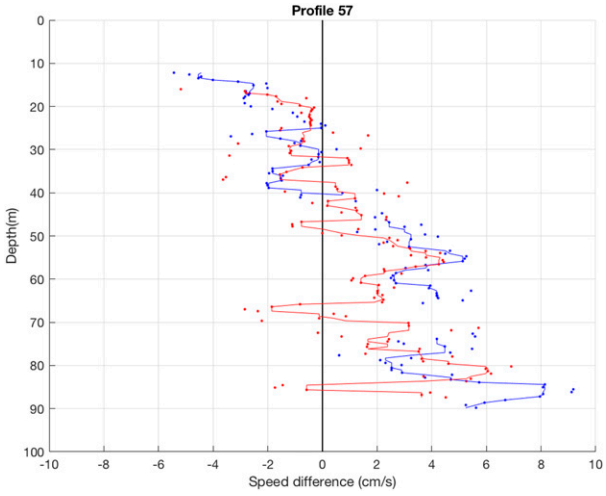

FIG. 10. Difference between acoustically tracked and method-predicted along-track vehicle speeds by depth for dive (blue) and climb (red) phases for profile 57. Solid lines indicate median-filtered differences using 5 samples (25 s). Black line highlights zero speed difference.

4. Discussion

Overall, we find the positional accuracy of the phase-based method using the buoyancy-driven HDM flight model to be quite good. Consistent with prior work from open-ocean deployments of gliders (Todd et al. 2017; Rudnick et al. 2018), we find the method can yield accurate velocities, on average, to 1 cm s^{-1} (or better) during the long dive and climb phases of a profile implying horizontal positional errors should grow slowly and linearly from known starting positions. For example, the dive phase of profile 69 (Fig. 1) shows no position error increase and in spite of errors introduced by misestimated apogee and climb-pump phase velocities, the profile accumulated only ~10 m of error over 30 mins, a position error rate of ~0.5 cm s^{-1}. Similarly, small position errors can be seen in profiles 60 and 62 (Fig. 8), recorded apparently during slack tide.

Accurate estimation of the flight-model and buoyancy parameters, especially vehicle volume, is critical to achieving this level of position accuracy. This investigation joins previous work (Frajka-Williams et al. 2011; Eriksen et al. 2001; Pelland et al. 2016; Bennett et al. 2019) demonstrating that the HDM-based regressions, utilizing measured pressure rate of change, are able to accurately resolve these parameters using routinely gathered flight data, especially when the vehicle explores different glide slopes. The inclusion into the regression cost function of measured along-track or horizontal vehicle speeds from velocimeters or onboard ADCPs, even intermittently, would further constrain and improve flight model parameter estimates, especially the drag coefficient.

On the relatively short and shallow dives investigated here, prior versions of the phase-based method assumed the horizontal velocity of the glider during the acceleration phases of a profile vanished, which distorted both the position and DAC estimates. As dives lengthen from 45 min to 8 h typical of 1000 m ocean deployments, the dive and climb phases dominate the profile and hence the position error introduced by the zero-speed assumption in these phases could be neglected. Directly solving the HDM momentum-balance equations now largely eliminates this source of error, although opportunities remain for improvement.

The principal residual source of position uncertainty is the variance of unresolved depth-dependent currents. Short of a model of such variable currents, bottom-mounted ADCPs or acoustic positioning systems such as the one used here will be required to detect the impact of these currents. Nevertheless, heuristically, with accurate flight parameters, glider position error via the HDM should grow roughly linearly from either GPS location during a profile at ~1 cm s^{-1} plus the average variance of DAC magnitude. For profiles of this deployment, which last 45 min, and a measured DAC variance of 0.5 cm s^{-1}, profile error estimates should amount to ~47 m, which, indeed, comfortably bounds the measured errors from the tracked dives. The 650 m RMS difference between flight model positions and acoustically derived positions for 1000-m dives in the Philippine Sea, noted in the introduction, are consistent with a 7 cm s^{-1} DAC variance, which is plausible for this highly energetic region where mean DACs were 18 cm s^{-1} and mean surface drifts were 42 cm s^{-1} (Van Uffelen et al. 2013).

Acknowledgments. We thank Geoff Shilling for several critical and well-timed observations and three anonymous reviewers for their insightful and helpful comments.
The Seaglider deployment on the Dabob Bay Acoustic Tracking Range was made possible with support from the Naval Undersea Warfare Center Division Keyport, with additional support provided by the Office of Naval Research (Award: N00014-17-1-2228, PI: Lora Van Uffelen and N00014-20-1-2040: National Institute for Undersea Vehicle Technology). This work was also supported by National Science Foundation Grant 1736217. Distribution A. Approved for public release: distribution unlimited. NUWC Keyport 20-011.

Data availability statement. As the data were collected on a U.S. Naval range, the datasets are available only upon request

Brought to you by University of Washington Libraries | Unauthenticated | Downloaded 06/08/21 05:35 PM UTC

and are subject to reporting conditions. Contact Lora Van Uffelen (loravu@uri.edu) for access.

APPENDIX

Determining HDM Flight Model Parameters Automatically

Separately we (JSB, FRS, CCE) developed a system (Bennett et al. 2019) that automatically solves the regressions to determine the hydrodynamic flight model parameters for *every* profile, incrementally, either during or postdeployment. Based on regression procedures developed by Eriksen et al. (2001) and Frajka-Williams et al. (2011), and similar to the method presented by Rudnick et al. (2013), the incremental, per-profile approach permits the system to detect and compensate for possible issues during a deployment that impact lift, drag, or buoyancy such as biofouling, sensor implosion, water incursion into vehicle fairings and syntactic foam, and ice sloughing. It can alert the pilot of possible issues with flight dynamics and improvements to navigation. The system can also be applied to completed Seaglider deployments.

Given predeployment measurement of the overall vehicle mass M, the goal of the system is to recover—via various regressions and using per-profile measurements of variable buoyancy-engine displacement [$V_{\mathrm{VBD}}(t)$], pitch ϕ, water temperature T, pressure p, and in situ seawater density—accurate values for the flight parameters for each profile as the deployment progresses, and hence recover accurate per-profile glider speeds and glide angles. The system performs, for each profile, several, sequenced regressions, described below, that minimize the overall root-mean-square difference in vertical velocity as measured by the pressure sensor versus the model (w_{rms}) of the profiles.

The hydrodynamic flight model describes the vehicle's steady flight in still water. To accurately estimate the flight parameters, the system employs heuristics to select profile data points that reflect steady flight. Measurements are discarded when the buoyancy engine is accelerating the vehicle during the flare, apogee, and climb phases. While Frajka-Williams et al. (2011) observed that some rolls could momentarily accelerate the vehicle (see their Fig. 6), this was likely due to pitch/roll mechanism coupling in that version of the vehicle. Analyzing rolls over many deployments we found this effect to be rare, small, and (even in the deployment they analyzed) negligible. Thus, data during rolls and small pitch adjustments are retained, which permits, for example, compass-calibration profiles employing constant roll to be used in the regressions.

The seawater temperature and in situ density used during the regressions are estimated from the uncorrected values returned from the conductivity–temperature (CT) instrument, before any speed-dependent thermal-inertia adjustments are performed; the typical impact of these adjustments for the purposes of estimating the flight parameters was found to be negligible. However, any conductivity anomalies (e.g., from bubbles or organisms) electrical spikes in temperature, etc. are removed. Other quality-control heuristics ensure that the pressure sensor, compass (for pitch), and the CT system are operating properly before using a profile's data. Finally, the system selects points where the measured vertical velocity is changing slowly, indicating relatively quiet water.

Overall, for new each profile, the system first determines any adjustments to buoyancy B by solving for changed volume (δV_0) and compressibility (κ) against an estimated reference volume (V_0), assuming the current best estimates of lift (a) coefficient, drag (b) coefficient, and compressibility. Second, the system determines the current flight regime itself, lift and drag in particular, using subsets of adjacent profiles selected at regular intervals.

At the beginning of a deployment the system assumes the vehicle's flight regime is characterized by a set of previously characterized default flight parameters by vehicle type (Seaglider, Deepglider, etc.). Subsequent regressions, however, can determine whether these parameter values are inappropriate and the system will reprocess previous profiles with improved sets of parameters.

Following Frajka-Williams et al. (2011), various sensitivity analyses indicate that variance in several parameters have negligible impact on speed estimates and can thus be estimated once and fixed for each vehicle type. For example, s is determined by hull shape. The induced drag parameter c was empirically estimated for each vehicle type by investigating near-stall and flat-spin behavior of some profiles; however, changing c even by an order of magnitude has very little impact on the a and b choices found by the system. The hull thermal expansion coefficient τ is dominated by the hull material and is treated as constant.

a. Determining Buoyancy Forcing: Estimating V_0, δV_0, and κ

Accurate determination of buoyancy forcing B for each profile requires estimating the buoyancy parameters V_0, δV_0, and κ in Eqs. (6) and (7).

Estimating the overall reference volume V_0 is done in two steps. While processing the first profile, the system estimates $V_{0,\mathrm{initial}}$ via M/ρ_{apo}, where ρ_{apo} is the measured in situ seawater density at apogee when $V_{\mathrm{VBD}}(t) = 0$. However, this initial assumption is often poor. Typically, there are bubbles trapped in the fairing that must be dissolved and the buoyancy system is not always adjusted to reflect true neutral buoyancy at apogee. Nevertheless, with a $V_{0,\mathrm{initial}}$ estimated, the system is able to then estimate, per profile, a δV_0 such that $(V_{0,\mathrm{initial}} - \delta V_0)$ reflects accurate vehicle density and therefore B.

Once the system estimates δV_0 values for several additional, early profiles with an assumed $V_{0,\mathrm{initial}}$ it then recomputes a final V_0 that would reduce the mean δV_0 value of these profiles to zero. The contributing profiles are then reprocessed against these modified $(V_0 - \delta V_0)$ values and all subsequent profiles assume this final V_0. A typical $V_{0,\mathrm{initial}}$ to final V_0 adjustment is $\sim$100 cm^3. Note that this procedure for estimating V_0 does not require an accurate vehicle mass M. As long as the measurement of in situ seawater density is

Brought to you by University of Washington Libraries | Unauthenticated | Downloaded 06/08/21 05:35 PM UTC

accurate, V_0 (and its associated per-profile δV_0) will be scaled properly to yield accurate buoyancies, which are a matter of relative, not absolute, densities.

Given a V_0, the system regresses δV_0 and then κ for each profile assuming the current best guess for lift and drag parameters in order to minimize the profile's w_{rms}. If the best guess for lift and drag change subsequently (see below) δV_0 and κ are automatically reestimated.

The compressibility κ of the vehicle is estimated using profiles to depths greater than 500 m where the effect on hull volume is appreciable. While dominated by the compressibility of the hull material (aluminum or carbon fiber) the mean value of κ was observed to change slightly per vehicle and per deployment, which likely reflects the different, combined compressibility of the hull, sensors, and fairing components.

b. Determining Lift and Drag Flight Regimes

The system combines profile data and buoyancy B estimates from subsets of adjacent profiles to estimate a single lift a and drag b pair that minimizes the combined w_{rms} of those profiles. To compare solutions between different sets of profiles and visualize the range of acceptable a–b pairs, the system implements this ''regression'' by solving w_{rms} at fixed a–b grid points. The result of one such grid search for the Dabob Bay deployment is shown in Fig. 3.

The choice of grid points reflects empirical observations of typical solution contours for a range of vehicle types. Overall the minimized w_{rms} solutions resembles a shallow bowl where most of the minimum solutions typically lie in the lower-left corner of the grid space. Very low-lift and high-drag pairs in the upper-left corner of the space often lead to substantially stalled solutions (indicated by black $\times$ symbols in Fig. 3).

The grid solution frequency varies as the deployment unfolds. Initially a search is performed every 4 profiles until profile 16, when it increases to every 8 profiles, until profile 40, when it increases to 16 profiles. More frequent early solutions quickly characterize the vehicle, permitting the pilot to adjust onboard flight parameters used for navigation. Later solutions permit detection of major changes in lift and drag coefficients. If the lift and drag values do change from the previous best guess from the last grid search (say, due to biofouling), each intervening profile's δV_0 and κ is provisionally recomputed using the new values of a and b; the a–b pair with the lowest w_{rms} is applied to each profile and the profile is reprocessed if needed using any changed flight parameters. In this way all profiles are constantly updated to reflect the best composite parameter estimates.

Frajka-Williams et al. (2011) observed that the drag coefficient b is better constrained by combining profiles with very different pitches angles and, therefore, angles of attack on the water. The system attempts to combine recent profiles that maximize the spread of pitch angles routinely obtained by those profiles. However, to minimize the time to compute a grid search, the system selects a subset of the profiles that maximizes the spread of pitch angles within those profiles and minimizes the number of total data points used in the search.

Empirically we find that a spread of vehicle pitch angles exceeding roughly 7° provide well-constrained values of b. For long transects between distant targets, the desired vehicle pitch requested on sequential profiles is often constant; however, steeply pitched profiles occur when attempting to achieve nearby waypoints/targets. If the set of profiles used in a grid search does not have a good spread of pitch angles the system alerts the pilot, recommending a steeply pitched profile. This can often be accomplished automatically on long transects by placing intermediate waypoints/targets along the transects. Short transect or bowtie sampling patterns, in contrast, provide steep profiles frequently enough to avoid the alert request. For example, the grid regression result shown in Fig. 3 is based on a pitch angle spread of 18°–28° where the steep profiles regularly occurred as the vehicle approached the transect navigation targets at the two ends of the Dabob Bay channel.

REFERENCES

Bennett, J. S., F. Stahr, and C. C. Eriksen, 2019: Determining Seaglider velocities automatically. University of Washington Tech. Rep., 50 pp., http://hdl.handle.net/1773/44948.

Eriksen, C. C., T. J. Osse, R. D. Light, T. Wen, T. W. Lehman, P. L. Sabin, J. W. Ballard, and A. M. Chiodi, 2001: Seaglider: A long-range autonomous underwater vehicle for oceanographic research. *IEEE J. Oceanic Eng.*, **26**, 424–436, https://doi.org/10.1109/48.972073.

Frajka-Williams, E., C. C. Eriksen, P. B. Rhines, and R. R. Harcourt, 2011: Determining vertical water velocities from Seaglider. *J. Atmos. Oceanic Technol.*, **28**, 1641–1656, https://doi.org/10.1175/2011JTECHO830.1.

Hubbard, R. M., 1980: Hydrodynamics technology for an advanced expendable mobile target (AEMT). University of Washington Applied Physics Laboratory Tech. Rep. APL-UW 8013, 34 pp.

Merckelbach, L., D. Smeed, and G. Griffiths, 2010: Vertical velocities from underwater gliders. *J. Atmos. Oceanic Technol.*, **27**, 547–563, https://doi.org/10.1175/2009JTECHO710.1.

——, A. Berger, G. Krahmann, M. Dengler, and J. R. Carpenter, 2019: A dynamic flight model for Slocum gliders and implications for turbulence microstructure measurements. *J. Atmos. Oceanic Technol.*, **36**, 281–296, https://doi.org/10.1175/JTECH-D-18-0168.1.

NOAA, 2020: Tides and currents. Accessed 16 December 2020, http://tidesandcurrents.noaa.gov/noaatidepredictions.html?id=9445269&units=metric&bdate=20180925&edate=20180927&timezone=LST/LDT&clock=12hour&datum=MLLW&interval=hilo&action=dailychart.

Pelland, N. A., C. C. Eriksen, and M. F. Cronin, 2016: Seaglider surveys at Ocean Station Papa: Circulation and water mass properties in a meander of the North Pacific Current. *J. Geophys. Res. Oceans*, **121**, 6816–6846, https://doi.org/10.1002/2016JC011920.

Rudnick, D. L., T. M. S. Johnston, and J. T. Sherman, 2013: High-frequency internal waves near the Luzon Strait observed by underwater gliders. *J. Geophys. Res. Oceans*, **118**, 774–784, https://doi.org/10.1002/jgrc.20083.

——, J. T. Sherman, and A. P. Wu, 2018: Depth-average velocity from Spray underwater gliders. *J. Atmos. Oceanic Technol.*, **35**, 1665–1673, https://doi.org/10.1175/JTECH-D-17-0200.1.

Brought to you by University of Washington Libraries | Unauthenticated | Downloaded 06/08/21 05:35 PM UTC

Snyder, W., L. Van Uffelen, and M. Renken, 2019: Effects of incorporating inertial measurements on the localization accuracy of the Seaglider AUV. *OCEANS 2019*, Marseille, France, IEEE, https://doi.org/10.1109/OCEANSE.2019.8867252.

Todd, R., D. Rudnick, J. T. Sherman, W. Owens, and L. George, 2017: Absolute velocity estimates from autonomous underwater gliders equipped with Doppler current profilers. *J. Atmos. Oceanic Technol.*, **34**, 309–333, https://doi.org/10.1175/JTECH-D-16-0156.1.

Van Uffelen, L. J., and Coauthors, 2013: Estimating uncertainty in subsurface glider position using transmissions from fixed acoustic tomography sources. *J. Acoust. Soc. Amer.*, **134**, 3260–3271, https://doi.org/10.1121/1.4818841.

——, B. M. Howe, E.-M. Nosal, G. S. Carter, P. F. Worcester, and M. A. Dzieciuch, 2016: Localization and subsurface position error estimation of gliders using broadband acoustic signals at long range. *IEEE J. Oceanic Eng.*, **41**, 501–508, https://doi.org/10.1109/JOE.2015.2479016.

Webster, S. E., C. M. Lee, and J. I. Gobat, 2014: Preliminary results in under-ice acoustic navigation for Seagliders in Davis Strait. *2014 Oceans*, St. John's, NL, Canada, IEEE, https://doi.org/10.1109/OCEANS.2014.7003070.

Brought to you by University of Washington Libraries | Unauthenticated | Downloaded 06/08/21 05:35 PM UTC